

Strength–Duration Relationship for Extracellular Neural Stimulation: Numerical and Analytical Models

David Boinagrov,^{1,2} Jim Loudin,^{1,3} and Daniel Palanker^{1,4}

¹Hansen Experimental Physics Laboratory, ²Department of Physics, ³Department of Applied Physics, and ⁴Department of Ophthalmology, Stanford University, Stanford, California

Submitted 12 April 2010; accepted in final form 6 August 2010

Boinagrov D, Loudin J, Palanker D. Strength–duration relationship for extracellular neural stimulation: numerical and analytical models. *J Neurophysiol* 104: 2236–2248, 2010. First published August 11, 2010; doi:10.1152/jn.00343.2010. The strength–duration relationship for extracellular stimulation is often assumed to be similar to the classical intracellular stimulation model, with a slope asymptotically approaching $1/\tau$ at pulse durations shorter than chronaxy. We modeled extracellular neural stimulation numerically and analytically for several cell shapes and types of active membrane properties. The strength–duration relationship was found to differ significantly from classical intracellular models. At pulse durations between 4 μ s and 5 ms stimulation is dominated by sodium channels, with a slope of -0.72 in log-log coordinates for the Hodgkin–Huxley ion channel model. At shorter durations potassium channels dominate and slope decreases to -0.13 . Therefore the charge per phase is decreasing with decreasing stimulus duration. With pulses shorter than cell polarization time (~ 0.1 – 1 μ s), stimulation is dominated by polarization dynamics with a classical -1 slope and the charge per phase becomes constant. It is demonstrated that extracellular stimulation can have not only lower but also upper thresholds and may be impossible below certain pulse durations. In some regimes the extracellular current can hyperpolarize cells, suppressing rather than stimulating spiking behavior. Thresholds for burst stimuli can be either higher or lower than that of a single pulse, depending on pulse duration. The modeled thresholds were found to be comparable to published experimental data. Electroporation thresholds, which limit the range of safe stimulation, were found to exceed stimulation thresholds by about two orders of magnitude. These results provide a biophysical basis for understanding stimulation dynamics and guidance for optimizing the neural stimulation efficacy and safety.

INTRODUCTION

Medical applications of extracellular neural stimulation continue to expand. They currently include cochlear implants to restore hearing to the deaf (House and Urban 1973; Zierhofer et al. 1995); visual prostheses to restore sight to the blind (Loudin et al. 2007; Rizzo and Wyatt 1997; Weiland et al. 2005; Zrenner 2002); bladder stimulators (Sawan et al. 1993); and deep brain stimulators to treat epilepsy, Parkinson's disease, dystonia, and chronic pain (Kringelbach et al. 2007). Understanding the mechanisms and dynamics of extracellular neural stimulation is very important for the development of electroneural interfaces, in general, and for the design of stimulation waveforms and electrode configurations for neural prosthetic implants, in particular.

The strength–duration relationship has been well established for intracellular stimulation, with several experimentally tested

theoretical models. The two most often cited formulas are those of Lapicque (1907)

$$I_{stim} = \frac{I_{rh}}{1 - 2^{-\tau/\tau_{ch}}} \quad (1)$$

and Weiss (1901)

$$I_{stim} = I_{rh} \left(1 + \frac{\tau_{ch}}{\tau} \right) \quad (2)$$

where I_{stim} is the minimum stimulation current necessary to elicit a spike, τ is stimulus duration, I_{rh} is the rheobase current, and τ_{ch} is chronaxy. The rheobase is the asymptotic constant level of current at long durations and chronaxy is the duration at which the stimulation strength becomes twice the rheobase. The Weiss equation provides a better fit to the experimental data in some cases (Bostock 1983; McIntyre and Grill 1998; Nowak and Bullier 1998), compared with the Lapicque equation (Dziubinska et al. 1983; Fozzard and Schoenberg 1972). Lapicque models transmembrane active membrane properties as a battery and resistor, whereas Weiss assumes a current source model. Both describe the intracellular stimulation as charging of the capacitive cell membrane, with the strength–duration curve having a constant rheobase level at long durations and asymptotic $1/\tau$ behavior for durations much shorter than chronaxy. However, the applicability of these equations to extracellular stimulation is unclear.

Outside of research settings, the most common type of neural stimulation is extracellular and yet its mechanisms and dynamics have scarcely been explored or described. Several experimental measurements of the strength–duration relationship have been reported (Jankowska and Roberts 1972; Jensen et al. 2005; Sekirnjak et al. 2006; Yoemans et al. 1988) and some computations have been performed (Greenberg et al. 1999; McIntyre and Grill 2002; McIntyre et al. 2002; Richardson et al. 2000). However, all such calculations and many of the measurements have focused on simple monophasic or biphasic stimuli not much shorter than chronaxy. Because the finite electrochemical capacitance of stimulation electrodes limits charge per phase, bursts of biphasic pulses can be used to increase the dynamic range of stimulation (Schoen and Fromherz 2008). A simple model of the system can provide significant guidance in the optimization of neural stimulation in the vast, multidimensional space of waveform parameters. The current study explores the basic mechanisms of extracellular stimulation to find fundamental analytical connections between properties of the ion channels and the strength–duration relationship.

Address for reprint requests and other correspondence: D. Boinagrov, Stanford University, Hansen Experimental Physics Laboratory, 452 Lomita Mall, Stanford, CA 94305 (E-mail: david86@stanford.edu).

METHODS

Model description

We used two different models of active cell membrane properties: the standard Hodgkin–Huxley (HH) model of a squid giant axon (Hodgkin and Huxley 1952) and a six-channel salamander retinal ganglion cell (RGC) model (Fohlmeister and Miller 1990). Three cell geometries were analyzed: an idealized planar cell with two uniformly polarized flat surfaces and more realistic spherical and cylindrical shapes, corresponding to the soma and unmyelinated axon or axon hillock. The HH model was applied to all three cell geometries, whereas the RGC model was applied to just the spherical cell. The planar HH model serves as a useful starting point because it effectively decouples geometric effects from the ion channel dynamics. The spherical and cylindrical models represent more realistic shapes and help to elucidate the effect of cell geometry on stimulation dynamics. All the models assumed a uniform electric field in the medium around the cell, which corresponds to experimental situations with either a large electrode close to the cell or a small electrode far from the cell.

Conductivity of ion channels is determined by the duty cycle of their open state (Liebovitch and Krekora 2002; Shapovalov and Lester 2004). Switching time between the open and closed states is likely to be one of the factors limiting the short end of the stimulus duration, since channels will not be able to respond to shorter voltage transients. Typically, measurement of the switching time in patch-clamp experiments with single ion channels is limited by the bandwidth of the current amplifiers to no better than a few hundred microseconds. A few measurements with ultrafast systems have shown that even with a time resolution of 3 μ s, the switching still appears instantaneous, i.e., bandwidth-limited (Hallermann et al. 2005; Shapovalov and Lester 2004). Molecular dynamics of the rotation of a helix in the ion channel protein, which determines the channel state, puts an estimate of the switching time as short as 30 ps (Liebovitch and Krekora 2002).

We calculated the strength–duration relationship within a range from 10 ns to 100 ms and have shown asymptotic behavior at each end of the range, predicting the trend beyond these limits.

HODGKIN–HUXLEY SQUID GIANT AXON MODEL OF ION CHANNELS. Although the HH model was initially developed to describe the active membrane properties of the squid giant axon, it was later found to be applicable to many other types of excitable cells with just a few modifications. In these variations, the potassium and the sodium channel parameters were adjusted and some additional types of channels were introduced. A detailed description of the HH model of active membrane properties is shown in APPENDIX A.

HH model of a planar cell. As a first approximation, we considered a simplified planar cell geometry in which two flat active membranes represent the sides of the soma, as shown in Fig. 1A. Since the side membrane is much smaller than the front and back planes, conductance of the side membrane can be neglected; thus any polarization falls entirely across the two membranes and a cytoplasm, represented by a resistor R . Although unrealistic, this geometry proves very useful in elucidating the roles of the individual ion channels in extracellular stimulation, decoupled from the geometrical complexities of real cells.

With the transcellular voltage V_{stim} and transmembrane voltages V_1 and V_2 , the system of Kirchhoff equations describing electric current in this circuit can be expressed as

$$C \frac{dV_1}{dt} = \frac{V_{stim} - V_1 + V_2}{R} + \bar{g}_K n_1^4 (E_K - V_1) + \bar{g}_{Na} m_1^3 h_1 (E_{Na} - V_1) + \bar{g}_L (E_L - V_1) \quad (3a)$$

$$C \frac{dV_2}{dt} = \frac{-V_{stim} + V_1 - V_2}{R} + \bar{g}_K n_2^4 (E_K - V_2) + \bar{g}_{Na} m_2^3 h_2 (E_{Na} - V_2) + \bar{g}_L (E_L - V_2) \quad (3b)$$

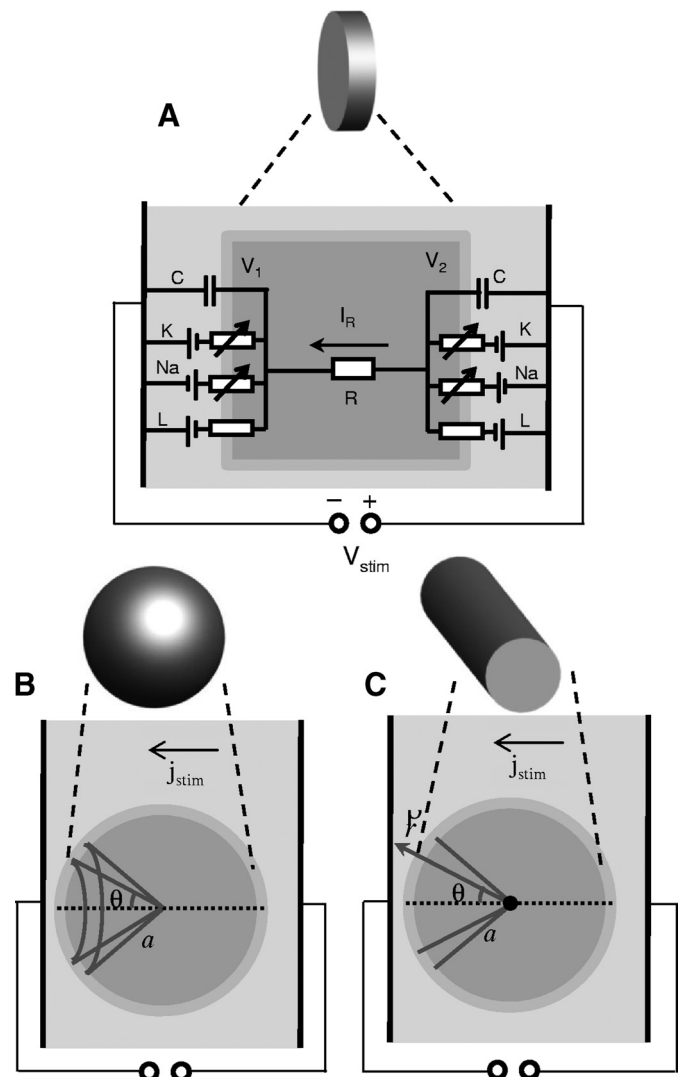


FIG. 1. The cell models. A: a planar cell, a short cylinder with its axis parallel to the stimulating electric field. The current through the intracellular resistor is $I_R = [V_{stim} - (V_1 + V_2)]/R$. B: a spherical cell of radius a . The membrane polarization caused by stimulation current j_{stim} is given by $\Delta V(\theta) = (3/2)\rho j_{stim} a \cos \theta$. C: a cylindrical axon of radius a , oriented across the field lines. The membrane polarization is $\Delta V(\theta) = 2\rho j_{stim} a \cos \theta$. In B and C the electrodes and cells are not drawn to scale: electrodes in the model are far from cells, creating a uniform current density j_{stim} far from the cell.

Here the potassium, sodium, and leakage ion currents are taken into account, as well as the capacitive and cytoplasmic currents. With constant parameter values n_i , m_i , and h_i ($i = 1, 2$), the solution to this system is an exponential decay to a steady state with $V_{stim} = V_1 - V_2$, and a characteristic time constant “cell polarization time” $\tau_p = RC/2$, where $C/2$ is the capacitance of the two membranes connected in series.

Without assuming constant parameter values, these constitute a self-consistent system of first-order nonlinear differential equations when combined with Eqs. A2a–A2g for activation and inactivation parameters (see APPENDIX A). We used the NDSolve function in the Wolfram Mathematica 6.0 software package to solve this system of equations numerically on a laptop PC. The threshold of cell spiking was determined to an accuracy of 1%. The maximum running time of the program for a single set of parameters was about 5 s.

HH model of a spherical cell. The simplicity of the planar model allows straightforward interpretation of the results and provides insight into the dynamics of extracellular stimulation. However, since it

implies rather unrealistic cell geometry, we also investigated a spherical cell, where the membrane polarization voltage gradually varies with position from a positive maximum to a negative minimum value. As shown in Fig. 1B, this change in polarization can be parameterized by the angle θ according to the equation (Cole 1968)

$$\Delta V(\theta) = \frac{3}{2} \rho_e a j_{stim} \cos \theta \quad (4)$$

where ρ_e is the extracellular media resistivity, a is the cell radius, and j_{stim} is the extracellular current density far from the cell.

For numerical computation in the case of a spherical cell, its surface was divided into 20 segments, each corresponding to $\pi/20$ radians of the whole $\theta = [0, \pi]$ interval. The membrane voltage across any one segment was approximated as constant (although time-dependent), with a value calculated for its middle angle; this voltage then determined the segment's ion channel conductivities and current flow. After the cell polarization is complete, the steady-state voltage V_i^s at the i th segment of the membrane is determined by the total intracellular charge and the modulation due to the stimulus current. During cell polarization in an external electric field the membrane voltage asymptotically approaches the steady-state values during the time τ_p , similar to the $RC/2$ time discussed in the previous section. Taking this into account, the equations for voltage V_i of the i th membrane segments $i = 1, 2, \dots, 20$ are

$$V_i^s = \frac{q}{C} + \frac{3}{2} \rho_e a j_{stim} \cos \theta_i \quad (5a)$$

$$\frac{dV_i}{dt} = \frac{V_i^s - V_i}{\tau_p} \quad (5b)$$

where q is the cell total internal charge per unit area, $\theta_i = -(\pi/40) + (\pi/20)i$ and V_i^s is the steady-state voltage of the i th membrane, as determined by the stimulus. The rate of change of the total intracellular charge is computed as the sum over all segments of the transmembrane currents j_i , with weight coefficients $\sin \theta_i$ proportional to the area of each section

$$\frac{dq}{dt} = \sum_{i=1}^{20} j_i \sin \theta_i \frac{\pi}{40} \quad (6)$$

The current density j_i in each point on the cell surface is computed as a sum of sodium, potassium, leakage, and capacitive currents for given point on the cell

$$j_i = \bar{g}_{Na} n_i^4 (E_K - V_i) + \bar{g}_{Na} m_i^3 h_i (E_{Na} - V_i) + \bar{g}_L (E_L - V_i) - \frac{dV_i}{dt} C \quad (7)$$

For more detailed j_i expression see APPENDIX A. The membrane conductivity is computed for each segment, assuming the HH active membrane properties. The cell polarization time can be estimated by the simple formula (Hibino et al. 1993)

$$\tau_p = aC(\rho_i + \rho_e/2) \quad (8)$$

With an intracellular and extracellular resistivity of $\rho_i = \rho_e = 70 \Omega \cdot \text{cm}$ (Foster et al. 1976; Geddes and Baker 1967) and cell radius $a = 5 \mu\text{m}$, this yields $\tau_p = 50 \text{ ns}$. Running this simulation for a single set of parameters on a laptop PC took about 3–4 min.

HH model of a cylindrical axon segment. We have also applied the HH model to cylindrical cell geometry, corresponding to a nonmyelinated axon in a uniform electric field. Here the axis of the cylinder is perpendicular to the stimulation current and is shown as a dot in the center of the cylinder in Fig. 1C. As in the spherical cell, the depolarization across the surface of the axon varies with position from

a positive maximum to a negative minimum value. The voltage modulation caused by the stimulation current is described by the following equation (see the derivation in APPENDIX B)

$$\Delta V(\theta) = 2\rho_e a j_{stim} \cos \theta \quad (9)$$

where ρ_e is the extracellular media resistivity, a is the axon radius, and j_{stim} is the stimulation current density far from the axon.

For numerical computation, the surface of the axon was divided into 20 pairs of segments, so that in each pair one was above and one symmetrically below the horizontal plane shown as a dotted line in Fig. 1C. Subsequently, the lower semicylinder behaved exactly like the upper one and thus only the upper 20 segments needed to be computed. Each segment covered $\pi/20$ radians. The membrane voltage across any one segment was approximated as the value calculated for its middle angle; this voltage determined the segment's ion channel conductivities and current flow. The equations for polarization of the membrane segments V_i ($i = 1, 2, \dots, 20$) are

$$V_i^s = \frac{q}{C} + 2\rho_e a j_{stim} \cos \theta_i \quad (10a)$$

$$\frac{dV_i}{dt} = \frac{V_i^s - V_i}{\tau_p} \quad (10b)$$

where q is the cell total internal charge per unit area and $\theta_i = -(\pi/40) + (\pi/20)i$. The membrane conductivity was computed for each segment, assuming HH active membrane properties. The rate of the change of the total intracellular charge was computed as a sum of all transmembrane currents, again weighted by the area

$$\frac{dq}{dt} = \frac{1}{20} \sum_{i=1}^{20} j_i \quad (11)$$

The current density j_i in each point on the cell surface can be computed by Eq. 7. For more detailed j_i expression see APPENDIX A. Running this simulation model for a single set of parameters on a laptop PC took about 3–4 min.

RETINAL GANGLION CELL MODEL. We also modeled tiger salamander (*Ambystoma tigrum*) retinal ganglion cells to assess the variability of stimulation dynamics with ion channel kinetics. Retinal ganglion cells are the target neurons in epiretinal visual prostheses (Hetling and Baig-Silva 2004; Weiland et al. 2005) and tiger salamanders are a commonly used model in the study of RGCs (Brivanlou et al. 1998; Kim and Rieke 2001). In this model (Fohlmeister et al. 1990) the membrane current is given by

$$j = \bar{g}_{Na} n^3 h (E_{Na} - V) + (\bar{g}_K n^4 + \bar{g}_A a^3 h_A + \bar{g}_{K,Ca})(E_K - V) + \bar{g}_{Ca} c^3 (E_{Ca} - V) + \bar{g}_L (E_L - V) - \frac{dV}{dt} C \quad (12)$$

which accounts for one sodium, one calcium, one leakage, and two types of voltage-activated potassium channels along with one calcium-activated potassium channel. Detailed expressions and numerical values of the parameters for this kinetic model are listed in APPENDIX C. Here, as in the previous section, a spherical cell was composed of 20 segments. The cell radius was taken as $a = 5 \mu\text{m}$ and external resistivity ρ_e was $7,900 \Omega \cdot \text{cm}$, in accordance with measurements of the RGC layer resistivity in the literature (Karwoski et al. 1985). Solving these RGC equations on a laptop PC took ≤ 10 min.

RESULTS AND DISCUSSION

Strength–duration relationship for the HH model

PLANAR CELL. Monophasic stimulus. The simplest stimulus was a single, rectangular monophasic voltage pulse, as shown in Fig. 2A. The corresponding strength–duration curves are

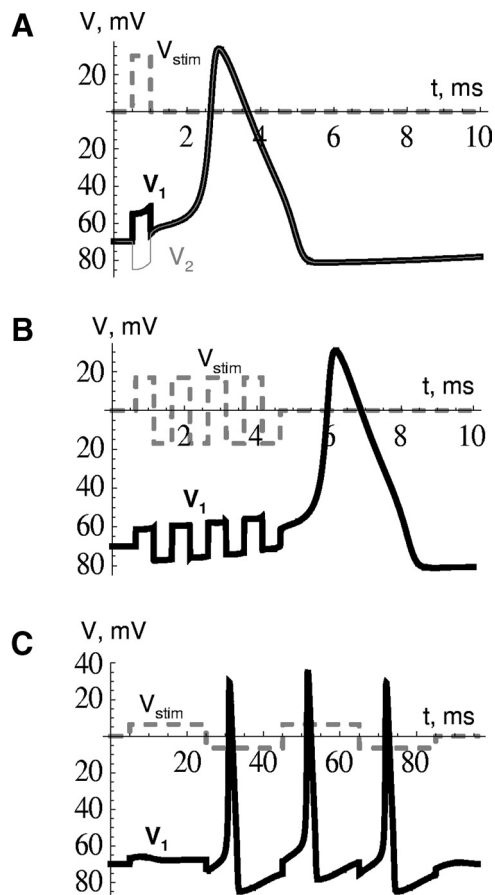


FIG. 2. Responses of the planar cell membranes to various stimuli. Solid bold lines depict the membrane voltage V_1 and dashed lines show the transcellular stimulation voltage for (A) monophasic stimulus (in addition to the bold line for V_1 , the thin line depicts V_2), (B) 4-biphasic bursts in the sodium-dominated regime, and (C) 2-biphasic bursts in the rheobase regime with the anodal break.

shown in Fig. 3, where the three solid lines represent the stimulation thresholds for different values of the cell polarization time $RC = 2\tau_p$: 1, 0.1, and 0.01 μ s. Naturally, these curves coincide at durations exceeding their respective polarization times, since the cell polarization effects are negligible at those durations. The computed strength-duration curves dramatically differ from the predictions of the classical Lapicque and Weiss Eqs. 1 and 2, which have a constant slope of -1 in log-log scale for subchronaxy durations. The Lapicque plot (dotted-dashed line in Fig. 3) with the same rheobase and chronaxy significantly deviates from the computed curves at short durations. The Weiss plot (not shown) slightly exceeds the Lapicque values within the 1- to 10-ms range and is slightly lower at pulse durations <0.3 ms.

All these computed curves have four distinct sections (see Fig. 3) corresponding to qualitatively different stimulation regimes.

1 The *rheobase regime*, for durations >5 ms, where stimulation threshold is constant.

2 The *sodium-dominated regime* for durations in the range of 4 μ s to 5 ms. The strength-duration curve here has a slope of -0.72 in log-log scale.

3 The *potassium-dominated regime* for durations in the range from τ_p to 4 μ s, with a log-log slope of -0.13 .

4 The *cell polarization-limited regime* for durations $<\tau_p$, with a slope of -1 .

Pulse durations corresponding to transitions between these regimes depend on the properties of ion channels and therefore will vary for various cell types.

Analysis of the stimulation regimes and their analytical models. In the absence of external stimuli the cell has a resting potential equal to -70 mV, the steady-state potential in the HH model in the absence of any stimulus. At this state there is a positive inflow of ions through the sodium and leakage channels, both of which tend to depolarize the cell. This inflow is compensated by the outflow of positive ions through the potassium channels, which tends to hyperpolarize the cell. The ion concentrations do not change in steady state because ion pumps compensate for the ion channel currents by actively moving ions across the cell membrane. When an external electric field is applied, the conductive intracellular medium equipotentializes, depolarizing the membrane on the cathodal side to $V_1 = -70 \text{ mV} + (V_{stim}/2)$ and hyperpolarizing the opposite membrane to $V_2 = -70 \text{ mV} - (V_{stim}/2)$. Sodium channels in the depolarized membrane are activated in response to the decreased transmembrane voltage. The resulting sodium inflow increases the intracellular potential, which in turn leads to further activation of the ion channels, accelerating the influx of sodium cations. If after the stimulus pulse is over the intracellular potential is sufficiently high to keep up this positive influx of ions, then the cell will continue depolarizing (increasing its intracellular potential), leading to spiking, as shown in Fig. 2A. As with the classical HH action potential, the spike ends when the sodium channels are inactivated and slower potassium channels activated, lowering the intracellular potential back to its resting value, thus ending the spike.

In the case of nonuniform distribution of ion channels on the cell surface the stimulation threshold will differ for cathodal and anodal stimuli. Stimulation threshold will be lower when the area of the cell with higher Na channel concentration is depolarized, compared with the opposite polarity, when this area is hyperpolarized. It occurs since the Na inflow on the depolarized side is responsible for the positive charge influx

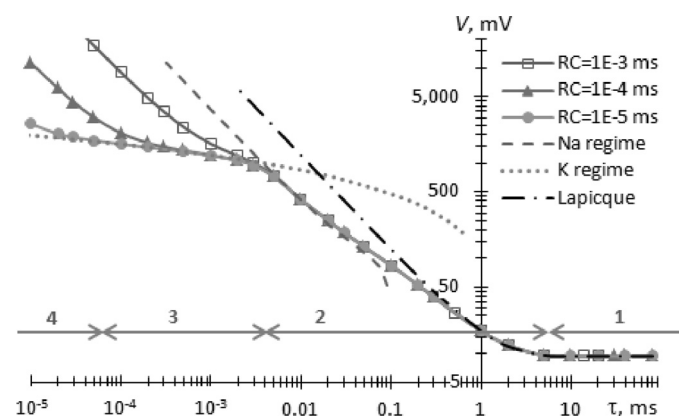


FIG. 3. Strength-duration relationships for monophasic stimulation of planar cells with different cell polarization times. The marked stimulation regimes are: 1 = rheobase; 2 = sodium-dominated; 3 = potassium-dominated; and 4 = polarization-limited (the boundary between regimes 3 and 4 is shown only for cell polarization time $[RC] = 10^{-4}$ ms). The dashed and dotted lines are the analytical approximations for the sodium- and potassium-dominated regimes, respectively, whereas the dash-dotted line shows the Lapicque curve with the same rheobase and chronaxy.

leading to subsequent spiking. This phenomenon has been observed experimentally: during epiretinal stimulation of the RGC cathodal stimulation threshold was lower than that of the anodal (Fried et al. 2006; Jensen et al. 2005). In the case of subretinal stimulation of RGCs, the anodal pulse had a lower threshold than that of the cathodal pulse (Jenson and Rizzo 2006). This asymmetry can be explained by nonuniform distribution of Na channels in the soma: the area of axonal hillock in RGCs (which is closer to the epiretinal surface) has a higher Na ion channel concentration, on average, than that of the soma (Fried et al. 2009; Wollner and Catterall 1986).

• **Rheobase regime:** In the rheobase regime the sodium charge inflow occurs mostly during the stimulation time. With decreasing pulse duration, stronger stimuli become necessary to activate the sodium channels enough for sufficient sodium uptake during the pulse to cause an action potential. This is the transition between the rheobase and the sodium-dominated regimes, shown in Fig. 3.

• **Sodium-dominated regime:** The Na channel activation begins during the stimulus and deactivation starts immediately after the stimulus. Equations A2a–A2h (see APPENDIX A) define an exponential decay in the sodium channel conductance after the stimulus with a time constant of

$$\tau_{Na}(V = -70 \text{ mV}) \cong \frac{1}{3} \tau_m = \frac{1}{3[\alpha_m(V) + \beta_m(V)]} \cong 0.08 \text{ ms} \quad (13)$$

near the resting potential. Although the channels are deactivated, the influx of ions continues to increase the intracellular potential by approximately $\Delta V \cong \Delta I_{Na} \cdot \tau_{Na} / C$, where ΔI_{Na} is the difference between sodium current density before and after the stimulation pulse and C is the membrane capacitance per unit area. The stimulation threshold is reached when the intracellular potential is increased by approximately $\Delta V_{th} = 6 \text{ mV}$ (this value was found by modeling intracellular stimulation with stimulus durations much shorter than chronaxy), which corresponds to a sodium current density increase of $\Delta I_{Na} = 75 \mu\text{A}/\text{cm}^2$. Since the resting value of sodium current density is $1 \mu\text{A}/\text{cm}^2$, this corresponds to a 76-fold increase in conductivity, which itself corresponds to a -fold increase in activation parameter m , from 0.053 to 0.23 ($\Delta m \approx 0.18$). Since the stimulus duration τ is much smaller than $\tau_{Na}(V = -70 \text{ mV}) \cong 0.08 \text{ ms}$, the change in membrane voltage V_1 during the stimulation pulse can be neglected. Assuming that depolarized membrane voltage V_1 stays constant at $V_1 = -70 \text{ mV} + (V_{stim}/2)$ during the stimulation pulse and that $m \ll 1$, we can find the first-order approximation for time dependence of m_1 from the differential Eqs. A2a, A2d, and A2e: $m_1(t) = m_1|_{t=0} + [t/\tau_m(V_1)]$. This yields an analytical expression for stimulus duration, generating the stimulation strength–duration relationship

$$\tau = \Delta m \cdot \tau_m(V_1) = \frac{0.18}{\alpha_m(V_1) + \beta_m(V_1)} \quad (14)$$

where $V_1 = -70 \text{ mV} + (V_{stim}/2)$. The dependence $\tau = \tau(V_{stim})$ is plotted as a dashed line in Fig. 3. Since the current influx during the stimulation period is neglected, this analytical approximation is valid only for pulse durations shorter than the Na channel deactivation time of 0.08 ms. As shown in Fig. 3, this analytical approximation matches well the asymptotic

behavior of the numerically computed strength–duration curves in the Na-dominated regime.

• **Potassium-dominated regime:** Cell depolarization can also be caused by the deactivation of potassium channels in the hyperpolarized membrane. With potassium channels deactivated, there is no longer any potassium outflow to balance the sodium and leakage inflow and thus the cell depolarizes. This effect triggers action potentials in the potassium-dominated regime, which occurs at stimulation durations shorter than those necessary for activation of the sodium channels. Figure 4A shows an example of the transmembrane voltage V_2 on the hyperpolarized side and the corresponding drop in its potassium channel conductivity. The membrane voltage in this example follows the stimulation voltage with an exponential decay waveform, with a characteristic time $RC/2 = 50 \text{ ns}$.

The K-channel deactivation takes place during the stimulus and activation begins when the stimulus is off. The potassium current decreased by the stimulus can trigger an action potential if it causes the intracellular potential to increase by the threshold value $\Delta V_{th} = 6 \text{ mV}$. For this to occur during the ion channel activation time τ_K , the current must decrease by $\Delta I_K \cong -(\Delta V_{th} C / \tau_K)$ during the pulse duration. At $V = -70 \text{ mV}$ the potassium time constant $\tau_K \cong 1/4 \tau_n = 1.4 \text{ ms}$. With $\Delta V_{th} = 6 \text{ mV}$, this yields $\Delta I_K \cong -4 \mu\text{A}/\text{cm}^2$. Since the potassium current in the resting state is $4.5 \mu\text{A}/\text{cm}^2$, this $4 \mu\text{A}/\text{cm}^2$ decrease brings it down to $0.5 \mu\text{A}/\text{cm}^2$. The potassium channel deactivation time constant provides an estimate of the strength–duration dependence of the stimulus in this regime

$$\tau = \tau_K \cong \frac{1}{4} \tau_n(V_2) = \frac{1}{4[\alpha_n(V_2) + \beta_n(V_2)]} \quad (15)$$

where $V_2 = -70 \text{ mV} - (V_{stim}/2)$ is the voltage on the hyperpolarized membrane. This dependence determines the strength–duration relationship of cell stimulation in this regime, as shown in Fig. 3. The analytical dotted line fits the computed strength–duration curve between $RC/2$ (cell polarization time) on the short end and $4 \mu\text{s}$ on the long end, where

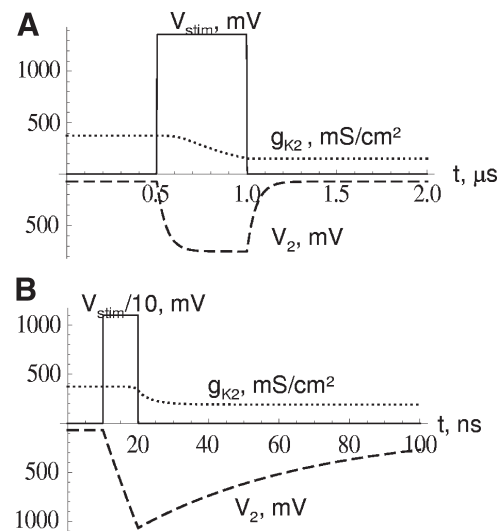


FIG. 4. Stimulation dynamics (A) in the potassium-dominated regime and (B) in the polarization-limited regime. The solid curve is the transcellular stimulation voltage V_{stim} ($V_{stim}/10$ for B); the dashed line is the hyperpolarized membrane voltage V_2 and the dotted line is the potassium channel conductivity g_{K2} .

sodium channel activation takes over. The transition between the sodium- and potassium-dominated regimes occurs at the intersection of the two curves defined by Eqs. 14 and 15.

For a given pulse duration, one of either the Na channel or the K channel that has a lower threshold dominates in stimulation. Time constants of the Na and K channels have different voltage dependences. At low voltages the Na channel activation on depolarized membrane is faster, and therefore it is the dominant process in spiking. However, at high voltages the potassium channel deactivation on the hyperpolarized side happens faster than the sodium channel activation on the depolarized side and thus potassium channels dominate at shorter durations.

● **Polarization-limited regime:** When stimulus duration does not exceed $RC/2$, the intracellular charge does not have enough time to redistribute from one membrane to the other during the pulse. For $\tau \ll RC$, the membrane capacitance charges up to only a small fraction of the applied stimulus voltage, so the RC circuit current remains approximately constant and is determined by the applied voltage V_{stim} divided by the resistance R . Thus at the end of the pulse the voltage on the hyperpolarized membrane has decreased by $V_{stim}\tau/RC$ (see Fig. 4B). After the stimulus the membrane voltages return to the resting potential with the decay time constant of $RC/2$. Since the potassium channels are deactivated at the fastest rate at the voltage minimum, it is in the neighborhood of the stimulus turnoff moment that the potassium channels are deactivated on the hyperpolarized side. Since the membrane's maximum hyperpolarization depends on the stimulus only in the combination $V_{stim}\tau/RC$, the strength-duration relationship in this regime has a simple inverse time dependence

$$V_{stim} \propto \frac{1}{\tau} \quad (16)$$

as can be seen on the left end of the curves plotted in Fig. 3.

Biphasic stimuli. Electrodes used for chronic stimulation typically cannot safely provide DC (Cogan et al. 2004), so in practical applications extracellular stimulation is generally performed using the charge-balanced biphasic stimuli. We explored the effects of both single symmetric biphasic pulses and biphasic bursts with no delays between the pulses (Fig. 2, B and C). As shown in Fig. 2B, the cell depolarization caused by subsequent pulses can be additive, thereby decreasing the threshold amplitude compared with the monophasic pulse shown in Fig. 2A.

The strength-duration curves for monophasic, 1- and 10-pulse biphasic stimuli are shown in Fig. 5, for $RC = 10^{-4}$ ms. Plotting the curves as a function of duration per phase highlights the effect of adding extra phases to the stimulation pulse. The regimes from Fig. 3 can be clearly seen on Fig. 5, with the second regime further divided into 2a and 2b, defined by whether the addition of extra phases decreases the stimulation threshold.

1 In the rheobase regime, with durations exceeding 5 ms, biphasic stimuli are more effective than monophasic, but additional biphasic pulses do not further decrease the threshold.

2a In the interval (0.1 ms; 5 ms) additional stimulation phases decrease the stimulation threshold. This is labeled the additive Na-dominated regime.

2b In the interval (0.004 ms; 0.1 ms) additional stimulation phases are detrimental—they increase the stimulation thresh-

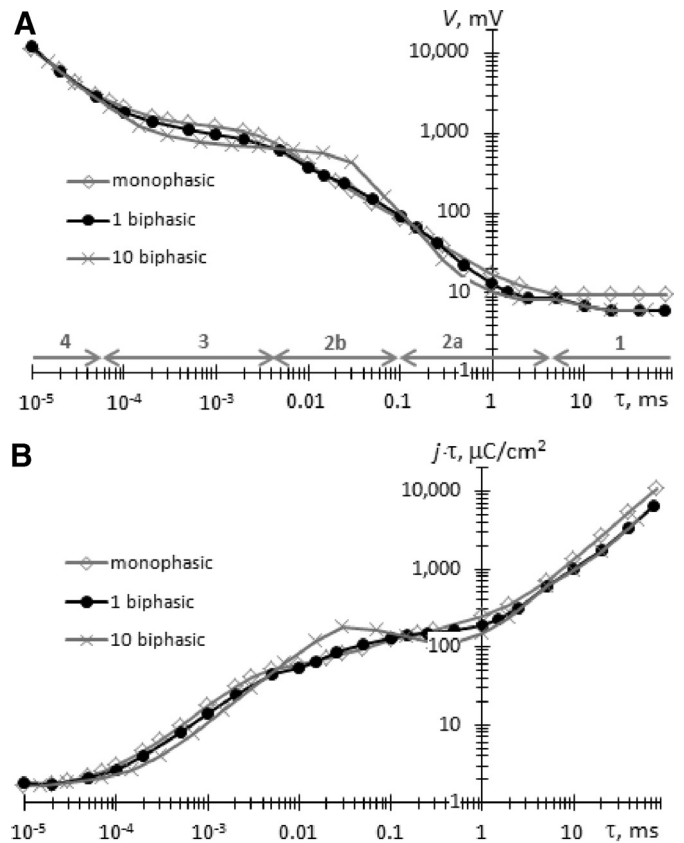


FIG. 5. The strength-duration relationship in terms of (A) stimulus voltage V_{stim} and (B) charge per phase. The curves were calculated for a planar Hodgkin-Huxley (HH) cell with polarization time $RC = 10^{-4}$ ms stimulated by monophasic, biphasic, and multiple biphasic “burst” stimuli. The marked stimulation regimes are: 1 = rheobase; 2a = additive sodium-dominated; 2b = sodium voltage reversal; 3 = potassium-dominated; and 4 = polarization-limited.

old. This regime corresponds to reversal of the Na driving force $E_{Na} - V$.

3 In the ($RC/2$; 0.004 ms) potassium-dominated regime additional stimulation phases again decrease the threshold.

4 In the $t < RC/2$ polarization-limited regime the number of stimulation phases has no effect on the stimulation threshold.

The first regime (rheobase) is illustrated in Fig. 2C, which shows the potential V_1 across the left membrane. Here we have a two-cycle biphasic stimulus of 20 ms per phase with amplitude just above the stimulation threshold. The cell spikes three times, when the stimulus voltage flips polarity, but does not spike during the first stimulating phase. This effect is known as an “anodal break” (Roth 1995). Just before the stimulus voltage changes, one side of the cell is hyperpolarized long enough (20 ms) to deactivate and deinactivate the sodium and potassium channels, thus decreasing their conductivity. After the stimulation polarity changes, the sodium channels are activated while staying partly deactivated and sodium ion inflow depolarizes the cell, whereas the slower potassium channels cannot activate quickly enough to balance the sodium ion inflow. This effect causes the stimulation threshold for biphasic pulses to be lower than that of monophasic ones, so long as the membrane has been hyperpolarized long enough for the potassium channels to deactivate and the sodium channels to dein-

activate. At the next voltage reversal the previously depolarized membrane now becomes hyperpolarized and vice versa; however, the ion flow dynamics is essentially the same. Since the spike is generated in each phase, the threshold does not change when additional phases are applied after the first biphasic stimulus.

In the additive Na-dominated regime 2a the influx of sodium ions during each phase additively contributes to the increase of the cell potential, as shown in Fig. 2B. Both sodium and potassium channels are deactivated on the hyperpolarized membrane, while at the same time the sodium channels are activated on the opposite, depolarized membrane. When the stimulus voltage switches polarity the hyperpolarized and depolarized sides swap, but cell depolarization continues. Thus lower amplitude is required to trigger an action potential with an increased number of stimulation phases.

In regime 2b the transmembrane voltage across the depolarized membrane becomes so high that it actually exceeds the sodium resting potential E_{Na} and, as a result, the sodium is actively pulled out of the cell, despite the concentration gradient pointing against such movement. This effect manifests itself as a negative current in Fig. 6B and corresponds to a change in sign of the $E_{Na} - V$ term in Eqs. 3a and 3b. Even though an action potential can still be triggered by the post-stimulus sodium influx, every additional phase of the stimulus contributes negatively to the cell potential (Fig. 6C), thereby increasing the stimulation threshold.

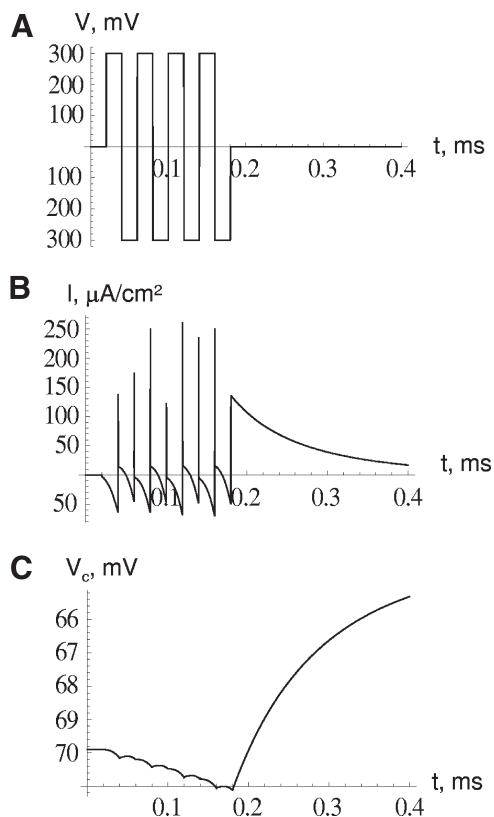


FIG. 6. Cellular response to a hyperpolarizing burst stimulus, showing (A) the stimulus, (B) total ionic current, and (C) cell potential $V_c = (V_1 + V_2)/2$. In this sodium voltage reversal regime each pulse draws out more sodium from the cell, so that additional pulses decrease stimulation efficacy (increase stimulation threshold).

The governing effect in the potassium-dominated regime is the deactivation of potassium channels on the hyperpolarized membrane, as described earlier in *Monophasic stimuli and Analysis of the stimulation regimes and their analytical models*. The effect of multiple phases is additive and thus a lower amplitude is required to trigger a spike with additional phases in the stimulus.

In the polarization-limited regime the cell does not have time to fully polarize in response to the applied stimulus. The dominant effect in this regime is the deactivation of potassium channels. Because of the short pulse duration, most of the depolarizing charge inflow occurs after the pulse is over. This inflow depends on the deactivation rate at which the cell is found after the stimulus. The deactivation rate of the potassium channels depends on the minimal voltage of the hyperpolarization (deactivation is faster at lower voltage), so the most significant deactivation occurs around this minimum. The minima of the subsequent phases are roughly of the same voltage and their corresponding deactivation is the same. Since the spike-eliciting current inflow takes place mostly after the pulse (burst) is over, and the current inflow rate depends on the deactivation rate, at which the cell membranes are at that moment, the number of phases or the history of how membrane channels were deactivated does not influence spiking. Thus the stimulation threshold does not depend on the number of phases.

Charge per phase. Chronic stimulation devices usually use electrodes made of platinum, titanium nitride, or iridium oxide (IrOx). All electrode materials have finite charge capacitances; exceeding their safe charge injection limits can lead to pH change, electrode delamination, bubble formation, and/or chemical tissue damage (Cogan et al. 2004). For square waveforms the finite charge density limits the product of pulse amplitude and duration of each phase. Usefully, it puts no limit on the number of biphasic charge-balanced pulses that may be applied. Charge density per phase of stimulus is calculated as $q = j\tau = (V/2a\rho)\tau$, where j is the density of current that flows in the electrolyte and creates the voltage drop V across the distance of the cell diameter a in the medium with resistivity ρ . Threshold charge density per phase for the HH planar cell model is plotted in Fig. 5B for the cell radius $a = 5 \mu\text{m}$ and $\rho = 70 \Omega \cdot \text{cm}$.

The amount of charge that can be safely delivered into electrolyte depends on the electrode material and geometry. For example, the positively biased IrOx electrode can safely deliver $\leq 3,500 \mu\text{C}/\text{cm}^2$ per phase (Beebe and Rose 1988), which is well above the values depicted on the graph on Fig. 5B beyond the rheobase region. Even larger charge density can be delivered via pipette electrodes with large metal surface exposed inside the pipette. Except for the polarization-limited regime, charge density threshold decreases with decreasing pulse duration. Therefore the charge injection is minimized at the shortest possible pulse duration, which is limited only by practically deliverable voltages and current densities.

SPHERICAL AND CYLINDRICAL CELLS. Figure 7 shows the calculated strength–duration curves for monophasic stimulation of a spherical cell of $10 \mu\text{m}$ in diameter. Unlike the constant positive and negative polarization values on the opposite sides of the planar cell model, membrane polarization in the spherical and cylindrical geometries varies continuously from the

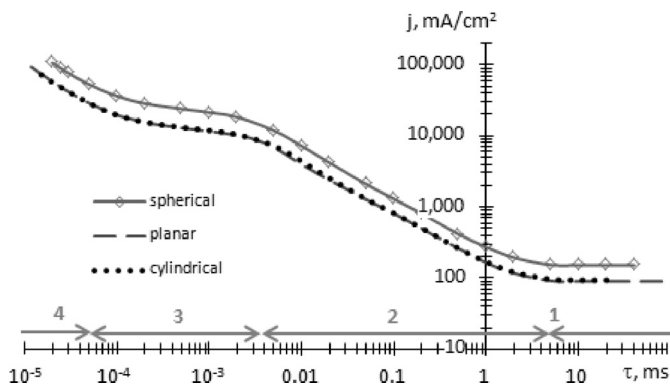


FIG. 7. Strength-duration curve for a spherical HH cell (solid) in units of current density stimulated by a monophasic pulse. The dashed and dotted curves are for the planar and cylindrical geometries, respectively, for the same stimulus. Simulations were performed for polarization time $\tau_p = 50$ ns.

maximum positive to the minimum negative values. However, the same stimulation regimes as with a planar cell (Fig. 3)—rheobase, sodium-dominated, potassium-dominated, and polarization-limited—can clearly be seen. The monophasic stimulation thresholds for the planar and cylindrical cells are lower than those of the spherical cell by a factor of about 1.7–1.8 throughout all durations. The difference is explained by the fact that membrane polarization in the spherical and cylindrical shapes varies from maximum positive to minimum negative along the cell surface, but has a constant value in the planar cell model. Additional contributing factors are the geometric difference in Eqs. 4 and 9, as well as averaging weights in Eqs. 6 and 11. In practice, the axon hillock is smaller than the cell soma, but has higher concentration of ion channels, which will yield a different stimulation threshold (Mainen et al. 1995; Tauc 1962). Here we focus on mechanisms of stimulation and limit our analysis to same sizes and active properties of the cell membranes.

The effect of additional stimulation phases on spherical and cylindrical cells is similar to that observed with the planar geometry. Phases are additive for long pulses in the sodium-dominated regime, but become less effective for shorter pulses in the voltage reversal regime. Additional phases again become more effective for even shorter pulses in the potassium-dominated regime, whereas there is nearly no difference in the polarization-limited regime.

Spherical model of the salamander retinal ganglion cell

The strength-duration curves for the spherical model of the tiger salamander RGC are shown in Fig. 8. The most striking difference between the RGC and HH models is that the RGC has both lower and upper stimulation thresholds. In addition, no spiking could be elicited below certain pulse duration. To elicit a spike, stimulus amplitude should be between the lower and upper stimulation limits. The stimulation upper limit has been experimentally observed on some neuronal cultures (Buitenweg et al. 2002). For long durations the upper stimulation limit is shown with a dashed line, since for these parameters the long stimulus itself interferes with the elicited spike, distorting it and causing the criterion for spiking to become poorly defined.

When stimuli exceed the upper limit, the cell becomes hyperpolarized due to sodium current reversal, in the manner

described earlier in *Analysis of the stimulation regimes and their analytical models* and SPHERICAL AND CYLINDRICAL CELLS. In the HH model the poststimulus sodium inflow can compensate for the previous sodium outflow and lead to spiking. However, in the RGC model the sodium channels deactivate faster and do not allow sufficient influx of sodium during the poststimulus period to elicit a spike. Also, the small potassium current in the resting state in the RGC model is insufficient for the potassium-dominated spiking.

For the RGC model, additional stimulation phases always decreased the threshold. The maximum improvement between the 1- and 10-pulse biphasic stimuli was twofold and was observed at 0.5 ms/phase. The charge per phase shown in Fig. 8B are well below the IrOx limit of $3,500 \mu\text{C}/\text{cm}^2$ per phase (Beebe and Rose 1988). The minimum charge per phase was achieved at around 0.1 ms (see Fig. 8B), with a corresponding 50-mV stimulus voltage drop across the cell.

Spike latency and stimulation range

A search for a stimulation upper limit in the HH model yielded a surprising result: instead of an upper boundary, there is a narrow gap in which no stimulation can be elicited, as shown in Fig. 9. For the fixed pulse duration a spike can be elicited between the stimulation lower limit and the lower limit of the gap or above the upper limit of the gap. For stimulus strengths just below the gap, the cell hyperpolarization caused by the sodium current reversal is compensated by the post-stimulation sodium influx via the still activated sodium channels. Inside the gap the hyperpolarization is so high that the poststimulus influx of sodium cannot overcome it. At still higher amplitudes (above the gap) the deactivation of the potassium channels on the hyperpolarized side becomes dominant and induces spiking. Subsequently, at pulse durations in the potassium-dominated regime there is no stimulation gap.

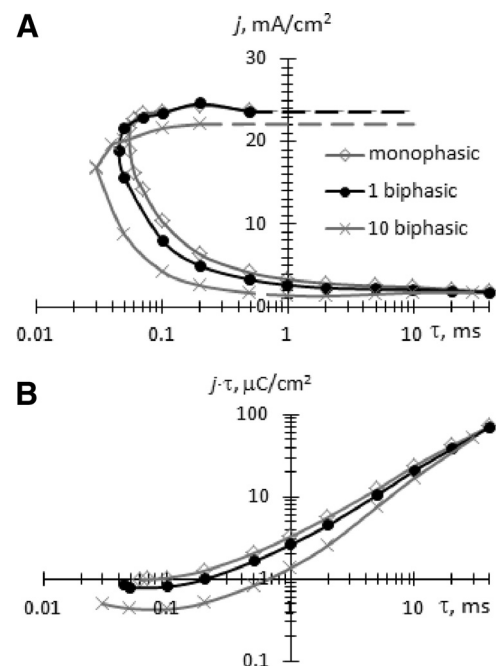


FIG. 8. Strength-duration curves for a spherical retinal ganglion cell (RGC) with monophasic, biphasic, and burst stimuli in terms of (A) current density and (B) charge density per phase (for lower stimulation threshold only).

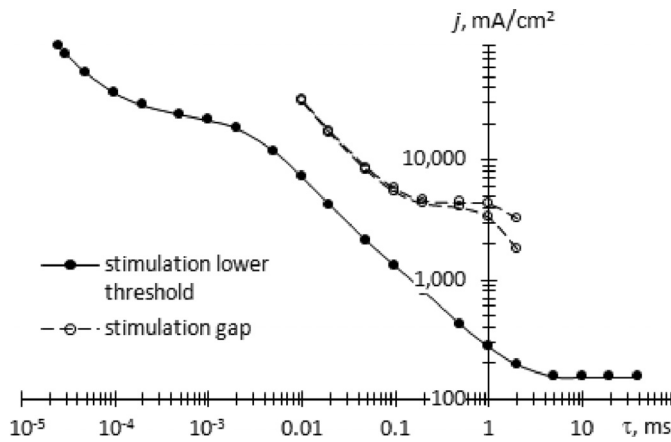


FIG. 9. Strength–duration relationship for a spherical HH cell with monophasic stimulus. The cell is stimulated everywhere above the stimulation lower threshold, except for the narrow stimulation gap.

The gap boundaries are not shown for long durations, since at these parameters the long stimulus itself interferes with the elicited spike, distorting it and causing the criterion for spiking to become poorly defined. The stimulation gap was also observed in the HH planar and cylindrical (axonal) geometries.

The latency of the elicited spike is defined as the time interval between the beginning of the stimulation pulse and the spike peak. Figure 10 shows spike latency as a function of stimulus intensity for a spherical RGC in the retina (resistivity of RGC layer $\rho = 7,900 \Omega \cdot \text{cm}$; Karwoski et al. 1985) and for a spherical HH cell in saline ($\rho = 70 \Omega \cdot \text{cm}$). For the RGC (left curve, $\tau = 0.1 \text{ ms}$) the latency first decreases rapidly as the stimulus increases above the threshold, as a result of more intense activation of the sodium channels. However, as the stimulus strength approaches the sodium voltage reversal threshold ($E_{Na} - V = 0$) the latency starts to increase, asymptotically approaching infinity at the upper stimulation limit. Similarly, the latency curve for the HH cell in the sodium-dominated regime ($\tau = 0.1 \text{ ms}$) exhibits well-defined upper and lower thresholds of stimulation. However, instead of an abrupt end to simulation, there is an additional branch of the curve to the right, which is separated by the narrow stimulation gap (indicated by an asterisk). At stimulus intensities just above the gap the latency decreases because the potassium channels deactivate more completely. Finally, the latency in-

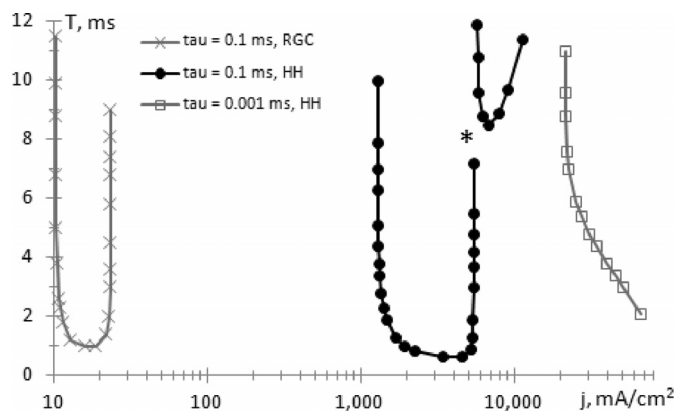


FIG. 10. Spike latency vs. stimulation strength for a monophasic pulse with stimulus durations shown in the legend. The curve on the left is for the spherical RGC in the retina, whereas the 2 curves on the right are for the HH spherical cell in saline. * depicts the stimulation gap.

creases again as stronger stimuli induce greater sodium-related hyperpolarization. The two branches of the HH latency curve directly correlate with the stimulation gap shown in Fig. 9. The left branch corresponds to the stimulation below the gap and the right branch to the stimulation above the gap. The spiking latency for the HH cell stimulated with a pulse of 0.001 ms is monotonically decreasing since this duration falls in the potassium-dominated regime, where the effect of the current reversal of the sodium channels is negligible and therefore the stimulation gap is absent.

Cellular hyperpolarization

In the Na voltage reversal regime (2b in Fig. 5) sodium ions are pulled out of the cell, leading to cell hyperpolarization. The degree of hyperpolarization can be controlled by the stimulus amplitude and duration. An example of a hyperpolarizing stimulus is shown in Fig. 11 for an HH planar cell. If the stimulus parameters fall in the stimulation gap (see previous section) then the poststimulus sodium ion influx cannot overcome this hyperpolarization and thus no spike can be elicited. Similar outcomes can be achieved with the RGC cell model by using stimulus amplitudes above the upper stimulation threshold. A burst waveform with variable amplitude can be designed to maintain a constant level of hyperpolarization to suppress cell spiking for a prolonged period of time.

Comparing modeled strength–duration curves with experimental stimulation and electroporation thresholds

Figure 12 shows the computed strength–duration relationships from SPHERICAL AND CYLINDRICAL CELLS and *Spherical model of the salamander retinal ganglion cell*, together with the published experimental data for rabbit RGCs (Jensen et al. 2005). These data were obtained using a large, 0.5 mm diam-

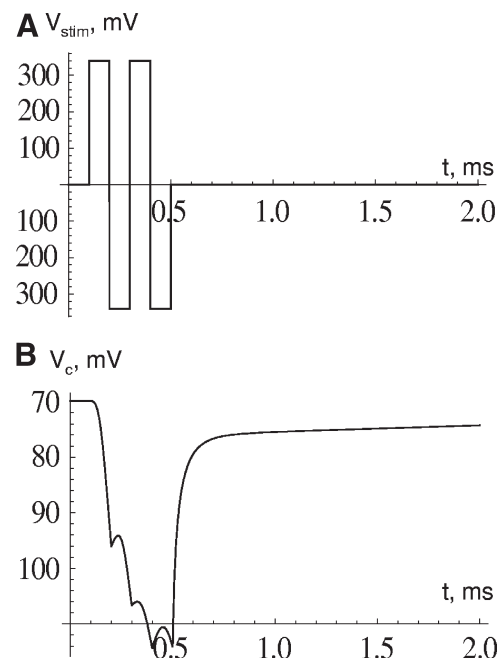


FIG. 11. The HH cell hyperpolarization induced by a burst biphasic stimulation: (A) the stimulus waveform; (B) cell potential $V_c = (V_1 + V_2)/2$ (planar cell model).

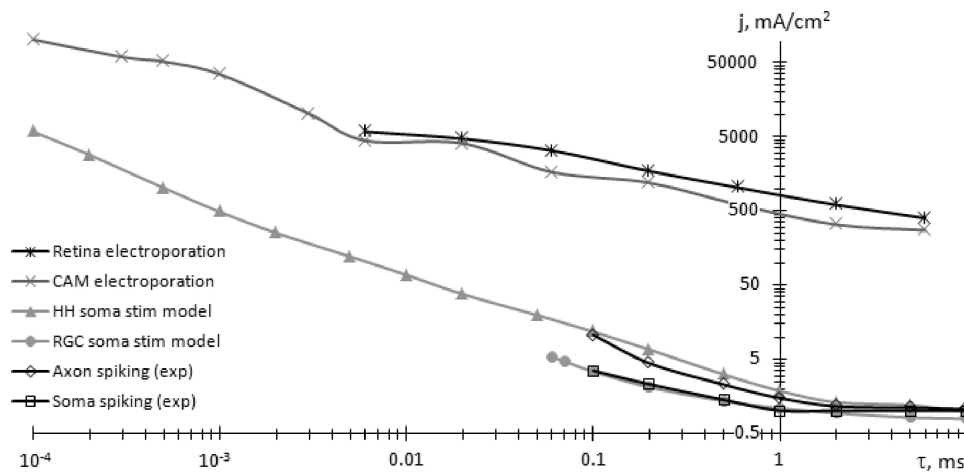


FIG. 12. Experimentally measured stimulation and electroporation thresholds plotted alongside the modeled stimulation thresholds for single biphasic pulses.

eter electrode that provides uniform current flow around the cell. The HH model curve was again computed assuming the radius $a = 5 \mu\text{m}$ and the RGC layer resistivity $\rho_e = 7,900 \Omega \cdot \text{m}$ (Karwoski et al. 1985). The corresponding cell polarization time for the HH soma stimulation model was $\tau_p = Ca[(\rho_i + \rho_e)/2] = 2 \mu\text{s}$ and thus the potassium-dominated regime is absent in this case. Since larger somas have lower stimulation threshold, they are more likely to be first detected in the extracellular recordings. Similarly, larger cells are typically selected for the patch-clamp or cell-attached recordings. According to the literature (Provis 1979), radius of the rabbit RGC soma can reach $15 \mu\text{m}$. To compare the experimental data with our modeling we used a soma radius of $15 \mu\text{m}$. As shown in Fig. 12, the modeled and experimental curves for the RGC soma match fairly well, with the short-end slopes in the range of -0.55 ± 0.02 . This value is significantly smaller than the slope of -1 , expected from the Weiss and Lapicque equations. The modeled HH soma stimulation curve shown has a slope of -0.72 in the sodium-dominated regime.

Electroporation, the formation of pores in cellular membranes due to a high electric field (Neumann et al. 1982), can result in cellular damage and thus limits the amplitude of the stimulating electric field. Electroporation thresholds taken from the literature (Butterwick et al. 2007) are plotted in Fig. 12 for comparison. These measurements were performed on chick chorioallantoic membrane (CAM) in vivo, as well as on porcine and chick retina in vitro. The electroporation thresholds are approximately two orders of magnitude higher than the stimulation thresholds for both HH and RGC cells, modeled and experimentally measured, leaving a sufficiently wide range for safe stimulation.

The ion channel parameters have been fitted by Hodgkin, Huxley, and others to the experimentally measured rate constants within the transmembrane voltage range of about 100 mV (a span of action potential). This study assumed that the same parameters can be applied for a wider range of the transmembrane voltages, corresponding to the intense extracellular stimuli. This assumption should be tested experimentally. Observation of the stimulation upper limit in RGCs (Buitenweg et al. 2002), predicted by the model for higher intensity stimuli, provides one evidence in support of our assumption. Since the Na current reversal takes place at membrane voltages of 35–45 mV, some of the most interesting predictions of the model, such as extracellular hyperpolariza-

tion suppressing spiking activity, do not require extraordinarily high voltages.

Conclusions

Since intracellular charge injection bypasses the ion channels and the whole cell membrane is under the same potential, most of the effects related to gradient of the electric field across the cell in extracellular stimulation and the associated ion channel dynamics are absent in intracellular stimulation, making its classical strength–duration dependence relatively simple. The numerical and analytical models of extracellular neural stimulation allowed elucidating the basic stimulation mechanisms and define the ranges of various dominant effects. It was found that in addition to the commonly considered sodium channel activation, cells can be stimulated by deactivating potassium channels on the hyperpolarized side, which results in a strength–duration relationship with a remarkably flat slope. It was also shown that the typical assumption that the strength–duration curve scales as $1/\tau$ at durations shorter than chronaxy is generally incorrect and such asymptotic behavior is reached only at extremely short durations, corresponding to the cell polarization-limited regime. The standard Hodgkin–Huxley model predicts no lower limit to spike-eliciting stimulus durations and no upper limit to stimulus strengths, although there is a narrow stimulation gap. However, a slightly more complex salamander RGC model predicts that stimulation is impossible below a certain pulse duration ($\sim 30 \mu\text{s}$), as well as above a certain stimulus amplitude (~ 20 times the rheobase level).

Both models of ion channels, HH and RGC, suggest that it is possible to hyperpolarize cells with appropriately designed burst extracellular stimuli. This phenomenon could be found useful for suppression rather than stimulation of neural activity. A computational model of extracellular neural stimulation can be applied to optimization of the stimulation waveforms, whereas further refinements can be made in the future by application of asymmetric stimuli, introduction of a more realistic geometry, with integrated axonal and dendritic structures and ion channels, specific for given neuron types and subcellular elements.

APPENDIX A

The HH squid giant axon active membrane properties model

In the original HH model, the transmembrane current has four terms

$$j = \bar{g}_K n^4 (E_K - V) + \bar{g}_{Na} m^3 h (E_{Na} - V) + \bar{g}_L (E_L - V) - \frac{dV}{dt} C \quad (A1)$$

where V is intracellular potential relative to the extracellular medium and $E_K = -82$ mV, $E_{Na} = 45$ mV, and $E_L = -59$ mV are the Nernst potentials of the potassium, sodium, and leakage ions. The fourth term in Eq. 3 describes the charging and discharging of the membrane capacitance $C = 1.0 \mu\text{F}/\text{cm}^2$ (Cole 1968). The first three terms describe the flow of potassium, sodium, and leakage ions across the cell membrane through the ion channels, which have variable conductances: $\bar{g}_K n^4$, $\bar{g}_{Na} m^3 h$, and, respectively. These conductances are limited by the maximum values of $= 36 \text{ mS}/\text{cm}^2$, $= 120 \text{ mS}/\text{cm}^2$, and $= 0.3 \text{ mS}/\text{cm}^2$ and are modulated by the activation (n , m) and deactivation (h) parameters. These parameters vary between 0 and 1 as functions of time and transmembrane voltage V , measured in mV

$$\frac{dx}{dt} = \alpha_x(1-x) - \beta_x x \quad \text{for } x = m, h, n \quad (A2a)$$

K⁺ channels

$$\alpha_n = 0.01 \frac{-V - 60}{\exp\left(-\frac{V}{10} - 6\right) - 1} \quad (A2b)$$

$$\beta_n = 0.125 \exp\left(-\frac{V}{80} - \frac{7}{8}\right) \quad (A2c)$$

Na⁺ channels

$$\alpha_m = 0.1 \frac{-V - 45}{\exp\left(-\frac{V}{10} - 4.5\right) - 1} \quad (A2d)$$

$$\beta_m = 4 \exp\left(-\frac{V}{18} - \frac{35}{9}\right) \quad (A2e)$$

$$\alpha_h = 0.07 \exp\left(-\frac{V}{20} - 3.5\right) \quad (A2f)$$

$$\beta_h = \frac{1}{\exp\left(-\frac{V}{10} - 4\right) + 1} \quad (A2g)$$

The time constants τ_x describe the rate of change of n , m , and h , as

$$\tau_x(V) = \frac{1}{\alpha_x(V) + \beta_x(V)} \quad \text{for } x = m, h, n \quad (A2h)$$

The experiments from which the ion channel parameters of HH model have been determined were conducted at 3–7°C.

APPENDIX B

Stimulation voltage distribution on a cylindrical surface

Let us consider a long conductive cylinder with an insulating boundary, located in a fluid with resistivity ρ in the presence of an external electric field $\vec{E} = -\nabla\varphi$, perpendicular to the cylinder's axis, which causes the current flow $\vec{j}_{stim} = \vec{E}/\rho$ (see Fig. 1C). The Poisson equation for the electric potential $\varphi = \varphi(r, \theta)$ in the extracellular medium is $\nabla^2\varphi = 0$. Due to the two-dimensional nature of the

problem, electric potential φ depends on the radius r and the polar angle θ , but does not vary with the distance z along the cylindrical axis. Therefore the Laplace equation can be written in polar coordinates as follows

$$\frac{1}{r} \frac{\partial}{\partial r} \left(r \frac{\partial \varphi}{\partial r} \right) + \frac{1}{r^2} \frac{\partial^2 \varphi}{\partial \theta^2} = 0 \quad (B1)$$

The boundary conditions for this problem are

$$\varphi_{r \rightarrow \infty} = -Er \cos \theta \quad (B2a)$$

$$j_r \Big|_{r=a} = \frac{1}{\rho} \left(-\frac{\partial \varphi}{\partial r} \right) \Big|_{r=a} = 0 \quad (B2b)$$

which state that 1) the influence of the cylinder is negligible at infinity, where electric field is uniform, and 2) that the radial component of electric current is zero at the insulating cylindrical surface.

We are looking for the solution of this equation in the form of $\varphi = Ar^\alpha \cos \theta$. Substituting this in Eq. B1 yields $\alpha = \pm 1$, so that the solution may be written as $\varphi = Ar \cos \theta + (B/r) \cos \theta$. The boundary conditions (Eqs. B2a and B2b) yield $A = -E$ and $B = -a^2 E$, where $E = \rho j_{stim}$.

Thus $\varphi(r, \theta) = -E[r + (a^2/r)] \cos \theta$ and $\varphi|_{r=a} = -2\rho j_{stim} a \cos \theta$. Since the steady-state voltage inside the cell is constant and independent of θ , the transmembrane voltage step (polarization) caused by the external current is

$$\Delta V = -\varphi_{r=a} = 2\rho j_{stim} a \cos \theta \quad (B3)$$

APPENDIX C

The salamander retinal ganglion cell model

The salamander RGC model simulates six ion channels (Fohlmeister et al. 1990)

$$j = \bar{g}_{Na} m^3 h (E_{Na} - V) + (\bar{g}_K n^4 + \bar{g}_A a^3 h_A + \bar{g}_{Ca} c^3 (E_{Ca} - V) + \bar{g}_L (E_L - V) - \frac{dV}{dt} C \quad (C1)$$

where $C = 1.0 \mu\text{F}/\text{cm}^2$, $E_K = -75$ mV, $E_{Na} = 35$ mV, $E_L = -60$ mV, $\bar{g}_K = 12 \text{ mS}/\text{cm}^2$, $\bar{g}_{Na} = 40 \text{ S}/\text{cm}^2$, $\bar{g}_{Ca} = 2.0 \text{ mS}/\text{cm}^2$, $\bar{g}_A = 36.1 \text{ mS}/\text{cm}^2$, $\bar{g}_{K,Ca} = 0.05 \text{ mS}/\text{cm}^2$, and $\bar{g}_L = 0.15 \text{ mS}/\text{cm}^2$.

The time evolution of the ion channel activation and inactivation parameters is given by

$$\frac{dx}{dt} = \alpha_x(1-x) - \beta_x x \quad (C2)$$

where $x = m, h, n, a, h_A$, and c . The parameters α_x and β_x are given by

$$\alpha_m = \frac{-0.6(V+30)}{\exp[-0.1(V+30)] - 1} \quad (C3a)$$

$$\beta_m = 20 \exp\left(-\frac{V+55}{18}\right) \quad (C3b)$$

$$\alpha_n = 0.4 \exp\left(-\frac{V+50}{20}\right) \quad (C3c)$$

$$\beta_n = \frac{6}{\exp[-0.1(V+20)] + 1} \quad (C3d)$$

Ca⁺ channel

$$\alpha_c = \frac{-0.3(V+13)}{\exp[-0.1(V+13)] - 1} \quad (C3e)$$

$$\beta_c = 10 \exp\left(-\frac{V+38}{18}\right) \quad (C3f)$$

K^+ channel

$$\alpha_n = \frac{-0.02(V + 40)}{\exp[-0.1(V + 40)] - 1} \quad (C3g)$$

$$\beta_n = 0.4 \exp\left(-\frac{V + 50}{80}\right) \quad (C3h)$$

A channel

$$\alpha_A = \frac{-0.006(V + 90)}{\exp[-0.1(V + 90)] - 1} \quad (C3i)$$

$$\beta_A = 0.1 \exp\left(-\frac{V + 30}{10}\right) \quad (C3j)$$

$$\alpha_{hA} = 0.04 \exp\left(-\frac{V + 70}{20}\right) \quad (C3k)$$

$$\beta_{hA} = \frac{0.6}{\exp[-0.1(V + 40)] + 1} \quad (C3l)$$

The experiments from which the ion channel parameters of RGC model have been determined were conducted at 22°C.

The conductivity of calcium-activated potassium channels is

$$g_{K,Ca} = \bar{g}_{K,Ca} \frac{([Ca^{2+}]_{int}/[Ca^{2+}]_{diss})^p}{1 + ([Ca^{2+}]_{int}/[Ca^{2+}]_{diss})^p} \quad (C4)$$

where $[Ca^{2+}]_{int}$ is the calcium intracellular concentration and the dissociation concentration is taken as $[Ca^{2+}]_{diss} = 10^{-3}$ mM and $p = 2$.

The intracellular concentration of calcium changes when calcium ions flow across the membrane. Calcium ions at concentrations above the resting level $[Ca^{2+}]_{res} = 10^{-4}$ mM are pumped out, a process modeled as an exponential decay with time constant $\tau_{Ca} = 50$ ms

$$\frac{d[Ca^{2+}]_{int}}{dt} = \bar{g}_{Ca} c^3 (E_{Ca} - V) \frac{S_i}{FW_i} - \frac{[Ca^{2+}]_{int} - [Ca^{2+}]_{res}}{\tau_{Ca}} - \frac{[Ca^{2+}]_{int} - [Ca^{2+}]_{int}}{\tau} \quad (C5)$$

$$[Ca^{2+}]_{int} = \frac{\sum_{i=1}^{20} S_i \cdot [Ca^{2+}]_{int}}{\sum_{i=1}^{20} S_i} \quad (C6)$$

Here S_i is the compartment surface area, W_i is the compartment volume, $F = 10^5$ C/mol is the Faraday constant, and $a = 5 \mu\text{m}$ is the cell radius.

The calcium resting potential can be calculated by the Nernst equation

$$E_{Ca} = 13.3 \text{ mV} \log \frac{[Ca^{2+}]_{ext}}{[Ca^{2+}]_{int}} \quad (C7)$$

where the external Ca concentration is $[Ca^{2+}]_{ext} = 16$ mM.

ACKNOWLEDGMENTS

We thank J. R. Huguenard for a stimulating discussion and insightful comments on the work.

GRANTS

This project was supported in part by National Eye Institute Grant 1R01-EY-018608, by Stanford Bio-X IIP grant, and by the Air Force Office of Scientific Research, grant FA9550-04.

DISCLOSURES

No conflicts of interest, financial or otherwise, are declared by the author(s).

REFERENCES

- Beebe X, Rose TL.** Charge injection limits of activated iridium oxide electrodes with 0.2 ms pulses in bicarbonate buffered saline. *IEEE Trans Biomed Eng* 35: 494–495, 1988.
- Bostock H.** The strength–duration relationship for excitation of myelinated nerve: computed dependence on membrane parameters. *J Physiol* 341: 59–74, 1983.
- Brivanlou IH, Warland DK, Meister M.** Mechanisms of concerted firing among retinal ganglion cells. *Neuron* 20: 527–539, 1998.
- Buitenweg JR, Rutten WLC, Marani E, Polman SKL, Ursum J.** Extracellular detection of active membrane currents in the neuron–electrode interface. *J Neurosci Methods* 115: 211–221, 2002.
- Butterwick A, Vankov A, Huie P, Freyvert Y, Palanker D.** Tissue damage by pulsed electrical stimulation. *IEEE Trans Biomed Eng* 54: 2261–2267, 2007.
- Cogan SF, Guzelian AA, Agnew WF, Yuen TG, McCreery DB.** Overpulsing degrades activated iridium oxide films used for intracortical neural stimulation. *J Neurosci Methods* 137: 141–150, 2004.
- Cole KS.** *Membranes, Ions and Impulses. A Chapter of Classical Biophysics.* Berkeley, CA: Univ. of California, 1968.
- Dziubinska H, Paszewski A, Trebacz K, Zawadzki T.** Electrical activity of the liverwort *Conocephalum conicum*: the all-or-nothing law, strength–duration relation, refractory periods and intracellular potentials. *Physiol Plant* 57: 279–284, 1983.
- Fohlmeister JE, Miller RF.** Impulse encoding mechanisms of ganglion cells in the tiger salamander retina. *J Neurophysiol* 78: 1935–1947, 1997.
- Foster KR, Bidinger JM, Carpenter DO.** The electrical resistivity of cytoplasm. *Biophys J* 16: 991–1001, 1976.
- Fozzard HA, Schoenberg M.** Strength–duration curves in cardiac Purkinje fibers: effects of liminal length and charge distribution. *J Physiol* 226: 593–618, 1972.
- Fried SI, Hsueh HA, Werblin FS.** A method for generating precise temporal patterns of retinal spiking using prosthetic stimulation. *J Neurophysiol* 95: 970–978, 2006.
- Fried SI, Lasker ACW, Desai NJ, Eddington DK, Rizzo JF 3rd.** Axonal sodium-channel bands shape the response to electric stimulation in retinal ganglion cells. *J Neurophysiol* 101: 1972–1987, 2009.
- Geddes LA, Baker LE.** The specific resistance of biological material: a compendium of data for the biomedical engineer and physiologist. *Med Biol Eng* 5: 271–293, 1967.
- Greenberg RJ, Velte TJ, Humayun MS, Scarlatis GN, de Juan E Jr.** A computational model of electrical stimulation of the retinal ganglion cell. *IEEE Trans Biomed Eng* 46: 505–514, 1999.
- Hallermann S, Heckmann S, Dudel J, Heckmann M.** Short openings in high resolution single channel recordings of mouse nicotinic receptors. *J Physiol* 563: 645–662, 2005.
- Hetling JR, Baig-Silva MS.** Subscribed content neural prostheses for vision: designing a functional interface with retinal neurons. *Neurol Res* 26: 21–34, 2004.
- Hibino M, Itoh H, Kinoshita K Jr.** Time courses of cell electroporation as revealed by submicrosecond imaging of transmembrane potential. *Biophys J* 64: 1789–1800, 1993.
- Hodgkin AL, Huxley AF.** A quantitative description of membrane current and its application to conduction and excitation in nerve. *J Physiol* 117: 500–554, 1952.
- House WF, Urban J.** Long term results of electrode implantation and electronic stimulation of the cochlea in man. *Ann Otol Rhinol Laryngol* 82: 504–517, 1973.
- Jankowska E, Roberts WJ.** An electrophysiological demonstration of the axonal projections of single spinal interneurons in the cat. *J Physiol* 222: 597–622, 1972.
- Jensen RJ, Rizzo JF 3rd.** Thresholds for activation of rabbit retinal ganglion cells with a subretinal electrode. *Exp Eye Res* 83: 367–373, 2006.
- Jensen RJ, Ziv OR, Rizzo JF 3rd.** Thresholds for activation of rabbit retinal ganglion cells with relatively large, extracellular microelectrodes. *Invest Ophthalmol Vis Sci* 46: 1486–1496, 2005.
- Karwoski CJ, Frambach DA, Proenza LM.** Laminar profile of resistivity in frog retina. *J Neurophysiol* 54: 1607–1619, 1985.
- Kim KJ, Rieke F.** Temporal contrast adaptation in the input and output signals of salamander retinal ganglion cells. *J Neurosci* 21: 287–299, 2001.
- Kringelbach ML, Jenkinson N, Owen SL, Aziz TZ.** Translational principles of deep brain stimulation. *Nat Rev Neurosci* 8: 623–635, 2007.

- Lapicque L.** Recherches quantitatives sur l'excitation électrique des nerfs traitée comme une polarization. *J Physiol Pathol Gen* 9: 620–635, 1907.
- Liebovitch LS, Krekora P.** The physical basis of ion channel kinetics: the importance of dynamics. In: *Volumes in Mathematics and Its Applications: Membrane Transport and Renal Physiology*, edited by Layton HE, Weinstein AM. Minneapolis, MN: Institute for Mathematics and Its Applications, Univ. of Minnesota, 2002, vol. 129, p. 27–52.
- Loudin JD, Simanovskii DM, Vijayraghavan K, Sramek CK, Butterwick AF, Huie P, McLean GY, Palanker DV.** Optoelectronic retinal prosthesis: system design and performance. *J Neural Eng* 4: S72–S84, 2007.
- Mainen ZF, Georges J, Huguenard JR, Sejnowski TJ.** A model of spike initiation in neocortical pyramidal neurons. *Neuron* 15: 1427–1439, 1995.
- McIntyre CC, Grill WM.** Sensitivity analysis of a model of mammalian neural membrane. *Biol Cybern* 79: 29–37, 1998.
- McIntyre CC, Grill WM.** Extracellular stimulation of central neurons: influence of stimulus waveform and frequency on neuronal output. *J Neurophysiol* 88: 1592–1604, 2002.
- McIntyre CC, Richardson AG, Grill WM.** Modeling the excitability of mammalian nerve fibers: influence of afterpotentials on the recovery cycle. *J Neurophysiol* 87: 995–1006, 2002.
- Neumann E, Schaefer-Ridder M, Wang Y, Hofschneider PH.** Gene transfer into mouse lymphoma cells by electroporation in high electric fields. *EMBO J* 1: 841–845, 1982.
- Nowak LG, Bullier J.** Axons, but not cell bodies, are activated by electrical stimulation in cortical gray matter I. Evidence from chronaxie measurements. *Exp Brain Res* 118: 477–488, 1998.
- Parzefall F, Wilhelm R, Heckmann M, Dudel J.** Single channel currents at six microsecond resolution elicited by acetylcholine in mouse myoballs. *J Physiol* 512: 181–188, 1998.
- Provis JM.** The distribution and size of ganglion cells in the retina of the pigmented rabbit: a quantitative analysis. *J Comp Neurol* 185: 121–138, 1979.
- Richardson AG, McIntyre CC, Grill WM.** Modeling the effects of electric fields on nerve fibers: influence of the myelin sheath. *Med Biol Eng Comput* 38: 438–446, 2000.
- Rizzo JF 3rd, Wyatt J.** Prospects for a visual prosthesis. *Neuroscientist* 3: 251–262, 1997.
- Roth BJ.** A mathematical model of make and break electrical stimulation of cardiac tissue by a unipolar anode or cathode. *IEEE Trans Biomed Eng* 42: 1174–1184, 1995.
- Sawan M, Duval F, Li JS, Hassouna M, Elhilali MM.** A new bladder stimulator, handheld controller and miniaturized implant: preliminary results in dogs. *Biomed Instrum Technol* 27: 143–149, 1993.
- Schoen I, Fromherz P.** Extracellular stimulation of mammalian neurons through repetitive activation of Na⁺ channels by weak capacitive currents on a silicon chip. *J Neurophysiol* 100: 346–357, 2008.
- Sekirnjak C, Hottowy P, Sher A, Dabrowski W, Litke AM, Chichilnisky EJ.** Electrical stimulation of mammalian retinal ganglion cells with multi-electrode arrays. *J Neurophysiol* 95: 3311–3327, 2006.
- Shapovalov G, Lester HA.** Gating transitions in bacterial ion channels measured at 3 μs resolution. *J Gen Physiol* 124: 151–161, 2004.
- Tauc L.** Site of origin and propagation of spike in the giant neuron of *Aplysia*. *J Gen Physiol* 45: 1077–1097, 1962.
- Weiland JD, Liu W, Humayun MS.** Retinal prosthesis. *Annu Rev Biomed Eng* 7: 361–401, 2005.
- Weiss G.** Sur la possibilité de rendre comparables entre eux les appareils servant à l'excitation électrique. *Arch Ital Biol* 35: 413–446, 1901.
- Wollner DA, Catterall WA.** Localization of sodium channels in axon hillocks and initial segments of retinal ganglion cells. *Proc Natl Acad Sci USA* 83: 8424–8428, 1986.
- Yeomans JS, Maidment NT, Bunney BS.** Excitability properties of medial forebrain bundle axons of A9 and A10 dopamine cells. *Brain Res* 450: 86–93, 1988.
- Zierhofer C, Hochmair-Desoyer I, Hochmair E.** Electronic design of a cochlear implant for multichannel high-rate pulsatile stimulation strategies. *IEEE Trans Rehabil Eng* 3: 112–116, 1995.
- Zrenner E.** The subretinal implant: can microphotodiode arrays replace degenerated retinal photoreceptors to restore vision? *Ophthalmologica* 216, Suppl. 1: 8–20, 2002.